Influence of the water vapor on the activity of CuO/SBA-15 SOx adsorbents

Gregory Guicheney, Sophie Dorge, Habiba Nouali, Bénédicte Lebeau, M. Soulard, J. Patarin, M. Molière, M. Vierling, A.C. Houdon, Jean-Francois Brilhac

▶ **To cite this version:**

Gregory Guicheney, Sophie Dorge, Habiba Nouali, Bénédicte Lebeau, M. Soulard, et al.. Influence of the water vapor on the activity of CuO/SBA-15 SOx adsorbents. Catalysis Today, 2021, 10.1016/j.cattod.2021.07.018 . hal-03442062

HAL Id: hal-03442062
https://hal.science/hal-03442062

Submitted on 22 Nov 2021

HAL is a multi-disciplinary open access archive for the deposit and dissemination of scientific research documents, whether they are published or not. The documents may come from teaching and research institutions in France or abroad, or from public or private research centers.

L'archive ouverte pluridisciplinaire **HAL**, est destinée au dépôt et à la diffusion de documents scientifiques de niveau recherche, publiés ou non, émanant des établissements d'enseignement et de recherche français ou étrangers, des laboratoires publics ou privés.

Influence of the water vapor on the activity of CuO/SBA-15 SO_x adsorbents

G. Guicheney[a,b,c,d], S. Dorge[a,c*], H. Nouali[b,c*], B. Lebeau[b,c], M. Soulard[e], J. Patarin[e], M. Molière[e], M. Vierling[f], A.C. Houdon[d], J.F. Brilhac[a,c]

[a] Université de Haute-Alsace (UHA), LGRE UR 2334, 68100 Mulhouse, France

[b] Université de Haute-Alsace (UHA), CNRS, IS2M UMR 7361, 68100 Mulhouse, France

[c] Université de Strasbourg, 67000 Strasbourg, France

[d] ADEME, 20 avenue du Grésillé, BP 90406, 49004 Angers Cedex 01, France

[e] Zéphir Alsace SAS, 68450 Brunstatt-Didenheim, France

[f] GE Energy, 20 avenue du Maréchal Juin, 90007, Belfort Cedex, France

[g] ADEME, 20 avenue du Grésillé, BP 90406, 49004 Angers Cedex 01, France

*Corresponding authors: sophie.dorge@uha.fr, habiba.nouali@uha.fr

Abstract

Both the performance and regenerability of SO_2 adsorbents made of CuO supported on SBA-15 ordered mesoporous silica were studied for a cyclic DeSOx process under wet and dry conditions. H_2O vapor decreases the performance of a 16 wt.% loading CuO/SBA-15 (16CuO/SBA-15) adsorbent along the adsorption/regeneration cycles performed at 400°C. Indeed, the SO_2 breakthrough adsorption capacity of this adsorbent after ten adsorption- regeneration cycles under wet conditions (5 vol.% of H_2O) decreases of 61% compared to the SO_2 performance obtained under dry conditions. The impact of the temperature as well as the CuO loading on the performance and regenerability of CuO/SBA-15 sorbents were also investigated under dry and wet conditions. XRD, TEM/EDX, N_2 physisorption characterizations of the adsorbents were performed after the last cycle to correlate the structural and textural properties of the adsorbents and therefore the copper species, with the performance of the

adsorbents. Increasing the temperature up to 450 °C with or without water increases the SO_2 adsorption capacity of the 16CuO/SBA-15 adsorbent with higher SO_2 adsorption capacity at 450°C with water than without water. In the presence of water vapor, the 8CuO/SBA-15 adsorbent presents the highest average loss of SO_2 adsorption capacity at the breakthrough of around 71 % when expressed in mg_{SO_2}/g_{CuO}, compared to the ones obtained with the 16CuO/SBA-15 and the 26CuO/SBA-15 adsorbents. The increase of the CuO loading up to 26 wt.%, shows that the contribution of the surface copper active phase highlighted by the desorption curves, decreases significantly for the highest CuO loading under wet conditions. Moreover, with or without water, the highest total SO_2 adsorption capacities obtained after the tenth cycle are observed for the lowest CuO loading (8 wt.% of CuO: 547 and 495 mg_{SO_2}/g_{CuO} without and with H_2O, respectively). These higher total SO_2 adsorption capacities could be explained by a better CuO phase dispersion on the SBA-15 support, which makes the copper active species more reactive especially with H_2O.

Keywords

DeSOx technology, CuO/SBA-15 adsorbents, adsorption/regeneration cycles, H_2O impact, H_2O/SO_2 competitive physisorption, CuO active phase agglomeration.

1. Introduction

It is widely acknowledged that air pollution generates detrimental consequences to biosphere. Thus, minimize the harmful human activity effects on air quality is a crucial challenge for our future and that of the planet. Among the atmospheric pollutants emitted by the burning fossil fuels used for energy production, transport and industrial activities, one finds the sulphur oxides (SO_x), compounds well known to be highly hazardous, not only towards human health (e.g. respiratory diseases) [1,2], but also towards fauna and flora (e.g. forest dieback, lake acidification and building erosion, all triggered by acid rains) [3]. To fight against these pollutants, various Flue-Gas Desulphurization (FGD) processes have

been developed. Based mainly on dry and wet scrubbing (using alkaline solids, solutions or suspensions) [4], these processes have greatly demonstrated their efficiency toward SO_x abatement. However, as listed in the BREF (Best available techniques REFerence documents) relating to large combustion plants [5], they present some drawbacks, in particular their high energetic consumption and cost and their tendency to generate large quantities of solid by-products with low recovery potential.

In order to comply with national and international guidelines [6,7] that are becoming increasingly more stringent with regard to the emissions of airborne pollutants and the means implemented to meet them, a SO_x trapping technology using functionalized adsorbents seems promising as an alternative to the common solutions. These SO_x adsorbents are usually made up of metal oxides such as CuO supported on Al_2O_3, ZrO_2, TiO_2, activated carbons or ordered mesoporous silica materials [8,9]. These latter materials have the ability to be regenerable and provide an FGD process without liquid or solid effluents production. In particular, copper oxide supported on an organized mesoporous SBA-15 silica, called CuO/SBA-15, has demonstrated a high SO_2 adsorption capacity under SO_2/N_2 atmosphere [10–13] along several adsorption/regeneration cycles without water. The set of chemical reactions involved in this regenerative FGD is:

(1) $SO_2 + ½\ O_2 \rightarrow SO_3$ oxidation of SO_2

(2) $SO_3 + MO \rightarrow MSO_4$ chemisorption of SO_3

(3a) $MSO_4 + 2H_2 \rightarrow SO_2 + M + 2H_2O$ reductive regeneration

(3b) $2MSO_4 + 3H_2 \rightarrow 2SO_2 + M_2O + 3H_2O$ reductive regeneration

The oxidation of SO_2 (reaction 1) is a prerequisite since SO_3 is chemisorbed by the metal oxide (reaction 2) that is then regenerated (reaction 3) under the form metal and/or metal oxide Cu_2O. The performance of this CuO/SBA-15 adsorbent is maintained in the presence of a complex mixture of gases containing the main pollutants of combustion exhaust (NO/NO_2, CO/CO_2). Furthermore, addition of NO/NO_2 in the flue gas slightly increased the SO_2 adsorption capacity of the CuO/SBA-15 adsorbent [13]. In addition, the CuO/SBA-15 adsorbent offers several other advantages such as:

- a SBA-15 support with a high thermal stability [14], a chemical inertia with respect to SO_2 [15] and a large specific surface area (700 - 1 200 m^2/g) [16] for a good dispersion of the active phase;
- a valorization of the SO_2 generated during the adsorbent regeneration step, e.g. in sulphuric acid [17,18] or pure sulphur production [19];
- a process which operates in the same thermal conditions than the ones of the exhaust flue gas (300 - 500 °C) during cyclic adsorption/regeneration [11–13,20].

Nevertheless, during combustion of solid and liquid fossil fuels, H_2O vapor is emitted. Therefore, the SO_2 adsorption/regeneration properties of the CuO/SBA-15 material in wet conditions must be also investigated in a perspective of a development of this FGD technology at industrial level. Indeed, some supported metal oxides used in numerous remediation techniques [21–27], see their performance impacted by the presence of water in the flue gas, which could deactivate their properties of remediation. This deactivation could be of reversible or irreversible nature with a return or not to the initial performance of the metal oxide after removal of water vapor from the flue gas, respectively. Iwamoto *et al.* [21] showed in their work on the removal of NO_x (i.e. $DeNO_x$) by SCR (Selective Catalytic Reduction) using hydrocarbons (C_2H_4, C_3H_6), a reversible deactivation of 35 % of a Cu-MFI catalyst, in presence of 3.9 % of H_2O at 500 °C. With NH_3 as reducer and MnO_x/Al_2O_3 as catalyst, Kijlstra *et al.* [22] observed an irreversible deactivation of 70 % in $DeNO_x$ catalytic activity, with 4 vol.% of H_2O at 150 °C. Liu *et al.* [23] also noticed a 10 % partial reversible deactivation (included 2 % of irreversible deactivation) with Cu-Mn/SAPO-34 $DeNO_x$ catalyst in presence of 10 vol.% of H_2O at 240 °C. As for Gholami *et al.* [24], they also related in their review on low temperature methane oxidation with Pd supported on Al_2O_3 or zeolites (H-Beta, H-TNU-10) in different wet and temperature conditions, a partial reversible deactivation of 5 to 86 % (included 2 to 68 % of irreversible deactivation) with 5-10 vol.% of H_2O at 400-600 °C. For a CO removal application with CuO/CeO_2 catalyst, Wu *et al.* [25] revealed that when 10 vol.% of H_2O is present in gas phase, an irreversible deactivation leads to increase the CO oxidation temperature about 40 to 50 °C to reach the same CO conversion and selectivity that at 40°C.

However, in some cases, the impact of water was positive with a promotion of the remediation activity. Indeed, Osaka *et al* [26] have noticed for a desulphurization process using MnO_2 as adsorbent, that the presence of 10 vol.% of H_2O in the exhaust gas containing 30-170 ppm of SO_2, at 200 °C, could lead to an SO_2 adsorption capacity gain of 82 % compared to the SO_2 adsorption capacity obtained without water. Moreover, Laguerie et Barreteau [27] noticed, in a FGD process with CuO/Al_2O_3 adsorbent, that for some SO_2 concentrations (2000 - 4000 ppm) in the flue gas at 300 °C, the presence of 6-10 vol.% of H_2O implies an increase of about 10 % of the desulphurization yield.

The aim of the present work is to assess the impact of the presence of H_2O in the gas phase, on the SO_2 trapping performance of the CuO/SBA-15 adsorbent during the cyclic SO_2 adsorption/regeneration and also to evaluate the influence of the temperature of the process and the content of the active phase in the adsorbent, on this performance.

2. Materials and methods

2.1. Preparation of the CuO/SBA-15 adsorbents

2.1.1. Reactants

The reactants for the CuO/SBA-15 adsorbents preparation were used as received without further purification: tetraethylorthosilicate (TEOS, Evonik) as silica precursor, triblock copolymer Pluronic® P-123 ($HO(CH_2CH_2O)_{20}(CH_2CH(CH_3)O)_{70}(CH_2CH_2O)_{20}H$, Sigma-Aldrich) as structure-directing agent, hydrochloric acid (HCl, 37 wt.%, Carlo Erba) as acid source and copper nitrate trihydrate ($Cu(NO_3)_2.3H_2O$, Sigma-Aldrich) as CuO precursor.

2.1.2. Synthesis of the SBA-15 ordered mesoporous silica support

The SBA-15 support was synthesized in a large amount, based on the procedure reported in our previous work [10] and optimized as follows: 196 g of Pluronic® P123 was dissolved in 1 121 g of HCl and 6 387 g of distilled water, at 45 °C for 12 h. Then, 425 g of TEOS was added to the solution, which was kept under stirring for 4 h at 45 °C. Afterward, the mixture was heated up to 90 °C for 18 h, under static mode and autogenous pressure. The white precipitate obtained was centrifuged, washed with distilled water until the washing water was at the pH of distilled water and dried overnight at 60 °C for 24 h in a ventilated oven. Lastly, in order to eliminate the porogen agent trapped in its mesopores, the as made SBA-15 material was calcined at 300°C under air flow in a muffle furnace with a temperature ramp of 1 °C/min up to 300 °C and a plateau of 4 h at 300°C. An amount of about 120 g of calcined SBA-15 was obtained (denoted SBA-300).

2.1.3. Impregnation of the SBA-15 ordered mesoporous silica support by the CuO active phase

The deposition of the CuO active phase on the SBA-15 support was achieved by wet impregnation in water [10–13,20]. Before to deposit the copper active phase, different samples were prepared to study the impact of each step of the impregnation process on the textural properties of the SBA-15 support:

- SBA-15 calcined at 300 °C and then at 500 °C (denoted SBA-500) to evaluate the impact of the temperature,
- SBA-15 calcined at 300 °C, then at 500 °C and shaped as described in the section 2.3. (denoted SBA-500-S) to evaluate the impact of shaping,
- SBA-15 calcined at 300 °C, then at 500 °C and pseudo-impregnated (denoted SBA-500-PI) to evaluate the impact of the impregnation step,
- SBA-15 calcined at 300 °C, then at 500 °C, pseudo-impregnated and shaped (denoted SBA-500-PI-S) to evaluate the impact of the impregnation step and shaping.

The N_2 physisorption analysis of these different samples shows that the textural properties are mainly impacted by the temperature of the calcination step (**Figure SI-1**). Indeed, a temperature of 500 °C, required to obtain the CuO active phase, applied on the SBA-15 support calcined at 300 °C, implies a

decrease of around 10 % of the total porous volume and specific surface area (S_{BET}). On the other hand, the pseudo-impregnation and shaping steps affect slightly the textural properties.

Then three different adsorbents, with a CuO loading of 8, 16 and 26 wt.%, were synthesized as follows: firstly, the amount of $Cu(NO_3)_2 \cdot 3H_2O$ precursor corresponding to the desired CuO loading was dissolved in 20 mL of distilled water. Then, 6 g of calcined SBA-15 material was added and the mixture was stirred at room temperature for 4 h. Next, the water was completely evaporated, under stirring, with a water bath heated at 60 °C. The resulting powder was completely dried at 60 °C for 24 h in a ventilated oven. Afterwards, it was calcined in a fixed-bed reactor (55 mm inner diameter), with 10 mm adsorbent bed thickness, under 150 NL/h of synthetic air flow (i.e. a Gas Hourly Space Velocity of 15 000 h^{-1}), with a temperature ramp of 1 °C/min up to 500 °C, followed by 6 h stage at 500°C and a cooling of 1 °C/min up to room temperature. The as-made adsorbents were designated as "XCuO/SBA-15", where X corresponds to the CuO wt.% loading, determined by X-Ray Fluorescence measurements. For example, the CuO/SBA-15 adsorbent containing 16 wt.% of CuO is denoted as 16CuO/SBA-15.

2.2. Characterization techniques

2.2.1. X-Ray Fluorescence

The determination of the CuO active phase loading in materials (**Table 1**) was performed with a X-Ray Fluorescence spectrometer Zetium from Panalytical and based on a homemade bulk CuO standard compound. The analysis was carried out on a sample compacted in 13 mm diameter tablet.

TABLE 1

Structural and textural properties of the SBA-15 support pretreated or not and of the fresh and spent CuO/SBA-15 adsorbents.

Sample	Specific surface area[a] ($m^2/g_{adsorbent}$)	Porous volumes ($cm^3/g_{adsorbent}$)			Average pores diameters[e] (nm)	Hexagonal lattice parameter[f] (nm)	Wall thickness[g] (nm)
		Total[b]	Micro.[c]	Meso.[d]			
Support							
SBA-300	750	0.80	0.19	0.61	6.0	-	-
SBA-500	660	0.71	0.16	0.55	5.6	-	-
SBA-500-S	630	0.67	0.16	0.51	5.6	-	-
SBA-500-PI	640	0.70	0.16	0.54	5.7	-	-
SBA-500-PI-S	630	0.68	0.16	0.52	5.7	-	-
Fresh adsorbents							
8CuO/SBA-15	430	0.49	0.14	0.35	4.0 / 5.9	10.2	4.3
16CuO/SBA-15	400	0.53	0.13	0.40	4.1 / 6.3	10.5	4.2
26CuO/SBA-15	400	0.51	0.13	0.38	4.0 / 6.2	10.6	4.4
Spent adsorbents							
8CuO/SBA-15, 400 °C							
0 vol.% H_2O	380	0.45	0.13	0.32	4.0 / 5.7	10.2	4.5
5 vol.% H_2O	390	0.46	0.13	0.33	4.0 / 5.7	10.1	4.4
16CuO/SBA-15							
350 °C							
0 vol.% H_2O	350	0.45	0.11	0.34	4.0 / 5.9	10.3	4.3
5 vol.% H_2O	340	0.45	0.11	0.34	4.0 / 6.0	10.4	4.5
400 °C							
0 vol.% H_2O	310	0.43	0.10	0.33	3.9 / 5.8	10.1	4.3
5 vol.% H_2O	300	0.42	0.10	0.32	3.9 / 6.0	9.8	3.8
450 °C							
0 vol.% H_2O	270	0.39	0.09	0.30	4.1 / 5.9	10.1	4.2
5 vol.% H_2O	310	0.44	0.10	0.34	4.1 / 6.1	10.0	3.9
26CuO/SBA-15, 400 °C							
0 vol.% H_2O	210	0.33	0.07	0.26	3.8 / 5.9	9.9	4.0
5 vol.% H_2O	190	0.30	0.06	0.24	3.8 / 5.8	9.8	4.0

[a] *Determined by the BET method [28]*
[b] *Total porous volume determined from the N_2 adsorbed volume at $p/p_0 = 0.90$*
[c] *Microporous volume determined from the N_2 adsorbed volume at $p/p_0 = 0.005$ [29]*
[d] *Mesoporous volume calculated from the difference between the total porous volume and the microporous volume*
[e] *Determined by the BJH method on the desorption branch [30]*
[f] *Determined from low 2θ angles XRD pattern*
[g] *Calculated from the difference between the hexagonal lattice parameter and the pore diameter*

2.2.2.X-Ray powder Diffraction (XRD)

The structural properties of the adsorbents were evaluated by X-Ray powder Diffraction (XRD). The analyses were realized in reflection mode on a X'Pert PRO MPD Powder diffractometer from Panalytical, equipped with a X'Celerator detector and a sample changer. Measurements were achieved

with $Cu_{K\alpha}$ radiation ($\lambda_{K\alpha}$ = 0.15418 nm), for 2θ angle values range from 0.02 to 70 ° (0.02 °/step, 220 s/step) and a fristed glass plate as sample holder.

2.2.3. Nitrogen adsorption/desorption measurements

The textural properties of the adsorbents were assessed by measurements of adsorption and desorption isotherms (at -196 °C) of nitrogen, carried out on a Micromeritics sorptometer model Tristar. Before measurements, samples were outgassed at 150 °C for 15 h under vacuum (10^{-3} mbar). The microporous and total pore volumes were measured at relative pressures p/p_0 = 0.005 (according to the work of Galarneau et *al.* [29]) and p/p_0 = 0.9, respectively. The mesoporous volume was calculated by microporous and total porous volumes difference. The specific surface area was determined by the BET (Brunauer-Emmett-Teller) method (in the range p/p_0 = 0.05 - 0.35) [28]. Mesopores size distribution was obtained by the BJH (Barrett-Joyner-Halenda) method applied on the desorption branch [30].

2.2.4. Transmission Electron Microscopy (TEM)

Transmission Electron Microscopy (TEM), Scanning Transmission Electron Microscopy (STEM) and Energy Dispersive X-ray (EDX) mapping images were obtained on a ARM-200F microscope from Jeol, equipped with a LaB_6 filament. First, samples were dispersed in chloroform and sonicated during 10 min. Next, two to three drops of the solution were deposited onto gold grids coated with a 5 nm thickness of holey carbon film.

2.3. $DeSO_x$ test: cyclic SO_2 adsorption and regeneration evaluation of the adsorbents

The fully automated system (**Figure 1**) used to evaluate the cyclic SO_2 adsorption and regeneration abilities ($DeSO_x$ performance) of the CuO/SBA-15 absorbents, has been amply described and validated in our previous work [10–13]. However, a study under wet conditions implied some adjustments:

- Integration of an evaporator system (Serv'Instrumentation equipment) which provides water vapor up to 10 vol.% (for a maximal gas flow rate of 30 NL/h) from a liquid mass flow meter (Horiba model) which injects liquid water into a heating chamber (at 120 °C). The steam produced is then conducted out with a carrier gas flow (O_2/N_2) controlled by a mass flow meter (Brooks model) towards the fixed bed where it is mixed with the SO_2/N_2 gas via an online static mixer.
- Setting up of a heated section (at 120 °C) composed with heated lines and a heated chamber above the furnace, it allows to keep the water in vapor form up to the entrance of the fixed bed reactor.
- Addition of a condenser using Peltier elements as cooling system to a better protection of the analyzer from water vapor.
- Use of a U-shaped fixed-bed reactor (6 mm inner diameter) provided with hand-operated gate valves and a fused silica frit (porosity: 100-160 µm). It allows to isolate the adsorbent under inert gas (N_2) after testing in order to realize specific characterization analyses.

Globally, the $DeSO_x$ adsorption/desorption tests were carried out on the adsorbent previously shaped in 32 mm diameter tablets (0.25 t/cm² for 2 min), manually crushed (with mortar and pestle) and sieved within the 250-355 µm range. A bed of 20 mm high of the shaped adsorbent was deposited on a frit in the U-shaped reactor. It was heated up to the desired temperature under pure N_2 flow within an electrical furnace, with a heating rate of 5 °C/min and followed by 1 h stage. Next, the adsorption step was launched during 10 800 s with an inlet gas stream composed of 250 ppm of SO_2 and 10 vol.% of O_2 diluted in N_2. For the tests performed under wet conditions, 5 vol.% of H_2O was added in the inlet gas stream, through the evaporator system. Afterward, the regeneration step was performed at the same temperature as the adsorption step, (isothermal process) under a reductive atmosphere composed of 0.5 vol.% of H_2 diluted in N_2, until 5 ppm of SO_2 is detected at the reactor outlet. A pure N_2 flow was imposed for 600 s between each adsorption and regeneration step. The outlet gas stream was analyzed online with an UV SO_2 adsorption analyzer (from Rosemount Analytical). The gas volumetric flow rate was maintained at 14 NL/h (i.e. a Gas Hourly Space Velocity of 25 000 h^{-1}) all along the test.

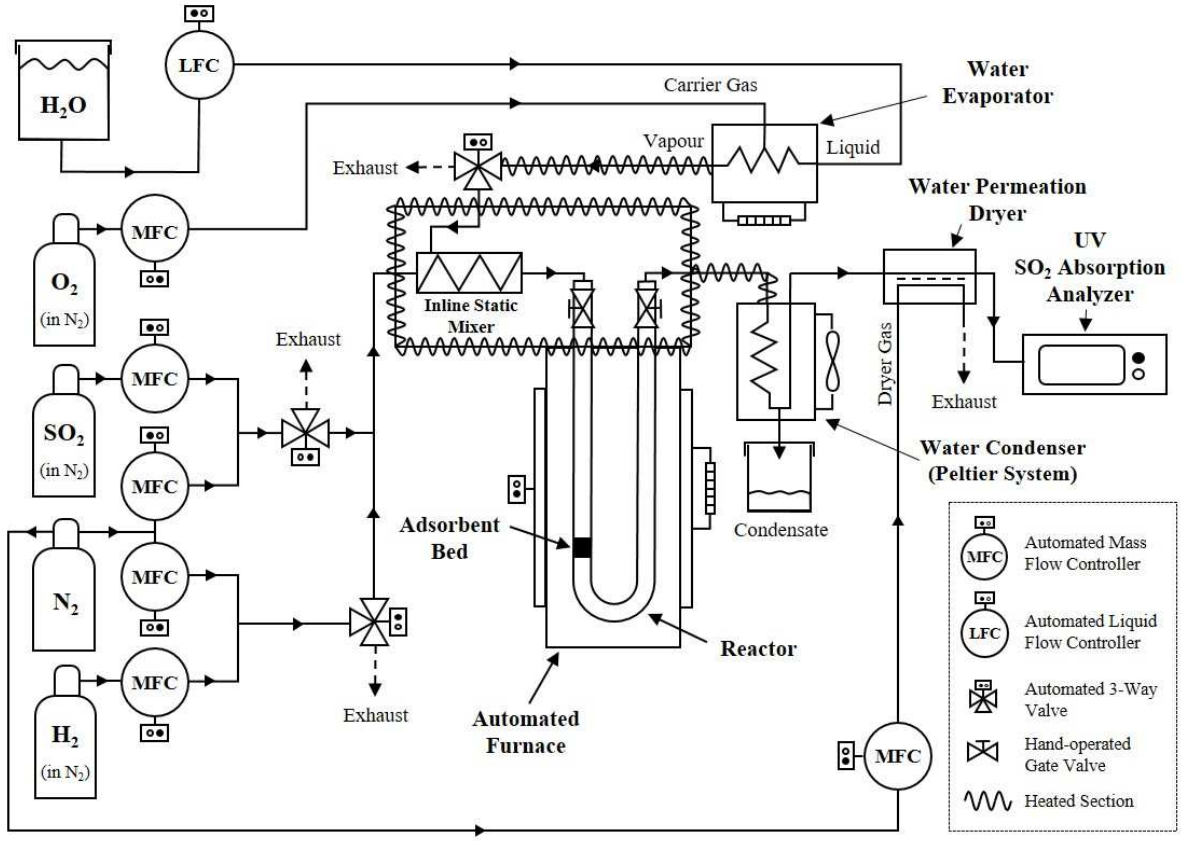

FIGURE 1

SCHEME OF THE AUTOMATED MULTICYCLE SO_2 ADSORPTION AND REGENERATION SYSTEM.

The $DeSO_x$ performance of the adsorbents were evaluated respectively according to the evolution of the SO_2 adsorption capacity at the breakthrough and the total SO_2 adsorption capacity throughout cycles. As represented in (**Figure 2**), these capacities were respectively determined from the integration of the SO_2 breakthrough curves (established during the adsorption step) and the integration of the SO_2 desorption curves (established during the regeneration step), according to equations **Erreur ! Source du renvoi introuvable.** and **Erreur ! Source du renvoi introuvable.**:

$$C_{SO_2}^{breakthrough} = \frac{F_v \times \int_{t_1}^{t_b}(C_0 - C)dt}{10^3 \times V_m \times m_{adsorbent}} \times M_{SO_2} \quad (4)$$

$$C_{SO_2}^{total} = \frac{F_v \times \int_{t_2}^{t_f} C\ dt}{10^3 \times V_m \times m_{adsorbent}} \times M_{SO_2} \quad (5)$$

where $C_{SO_2}^{breakthrough}$ and $C_{SO_2}^{total}$ (in $mg_{SO_2}/g_{adsorbent}$) are the SO_2 adsorption capacity at the breakthrough and the total SO_2 adsorption capacity of the adsorbent, respectively. F_v (in NL/h) is the gas volumetric flow rate. C_0 and C (in ppm) are respectively the inlet and outlet SO_2 concentration. t_1 and t_2 (in h) are the starting time of the adsorption step and the regeneration step, respectively. t_b and t_f (in h) are the time at the SO_2 breakthrough (when 5 ppm of SO_2 is detected from the analyzer) and the final time of the regeneration step, respectively. V_m is the molar volume of a gas (22.4 L/mol at 0 °C and 1 atm). $m_{adsorbent}$ is the mass of adsorbent within the fixed-bed (in g). M_{SO_2} is the molecular mass of SO_2 (64 g/mol).

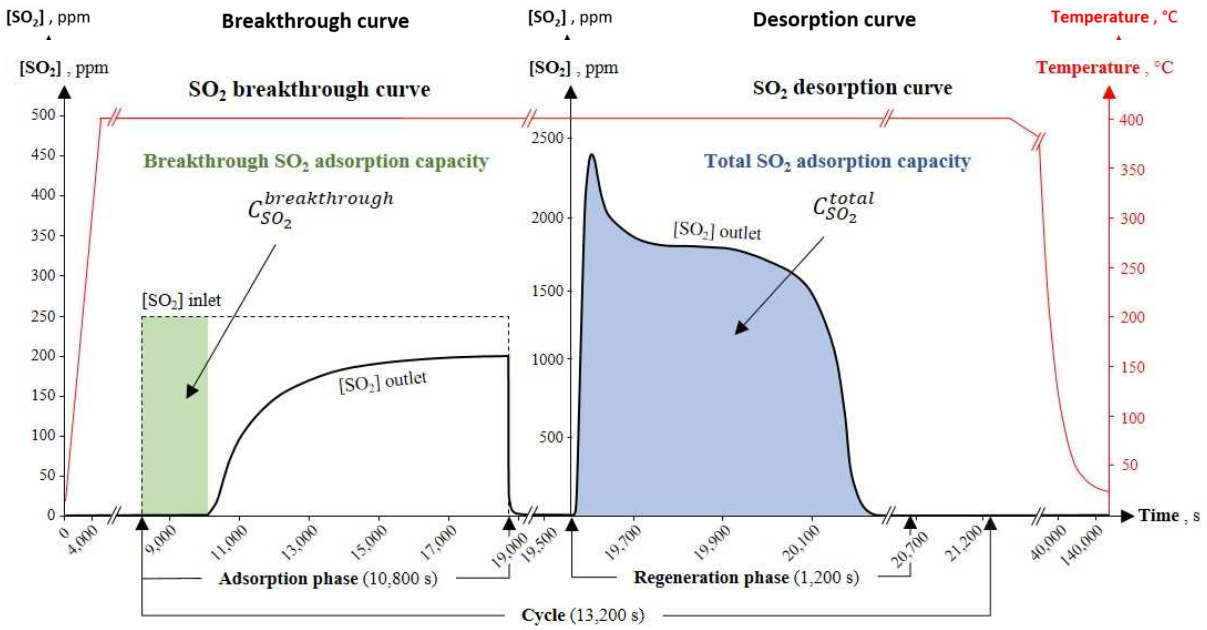

FIGURE 2

Determination of the SO_2 adsorption capacity at the breakthrough and the total SO_2 adsorption capacity of the materials (representation of one adsorption /regeneration cycle).

3. Results and discussion

3.1. SO_x trapping performance of the CuO/SBA-15 adsorbents under wet conditions

3.1.1. SO_x trapping performance of the 16CuO/SBA-15 adsorbent under wet conditions

The first goal of this study is to evaluate the impact of the presence of water vapor in the inlet gas stream, on the SO_x trapping performance of a 16CuO/SBA-15 adsorbent along cycling experiments. This adsorbent was chosen as a reference material because it has been widely studied in our previous works [10–13,20]. The $DeSO_x$ tests were performed at 400 °C, over ten successive SO_2 adsorption/regeneration cycles, without or with 5 vol.% of H_2O during the adsorption step. SO_2 breakthrough curves (adsorption step) and desorption curves (regeneration step) and the evolution of the SO_2 breakthrough adsorption capacity $C_{SO_2}^{breakthrough}$ and the total SO_2 adsorption capacity $C_{SO_2}^{total}$, are reported in **Figure 3** and **Figure 4,** respectively**.**

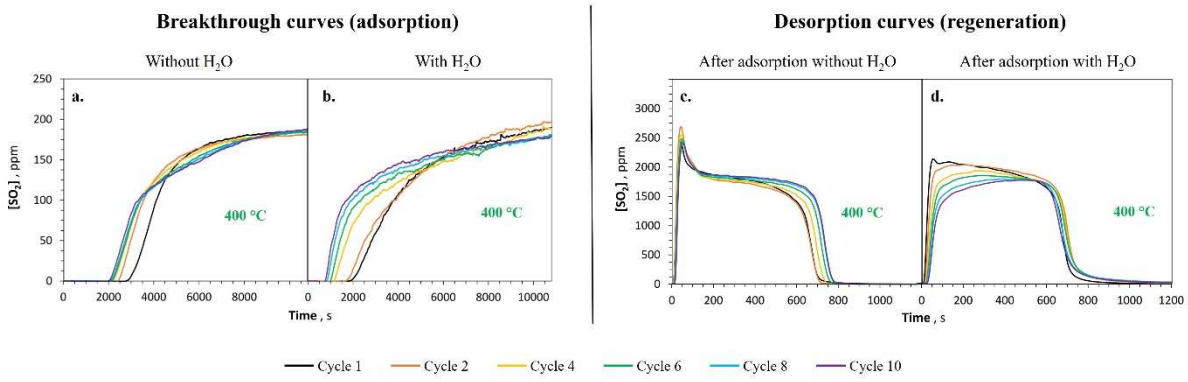

Figure 3

SO_2 breakthrough (left) and desorption (right) curves of the 16CuO/SBA-15 adsorbent, submitted to ten SO_2 adsorption/regeneration cycles, at 400 °C, with and without H_2O during the adsorption step.

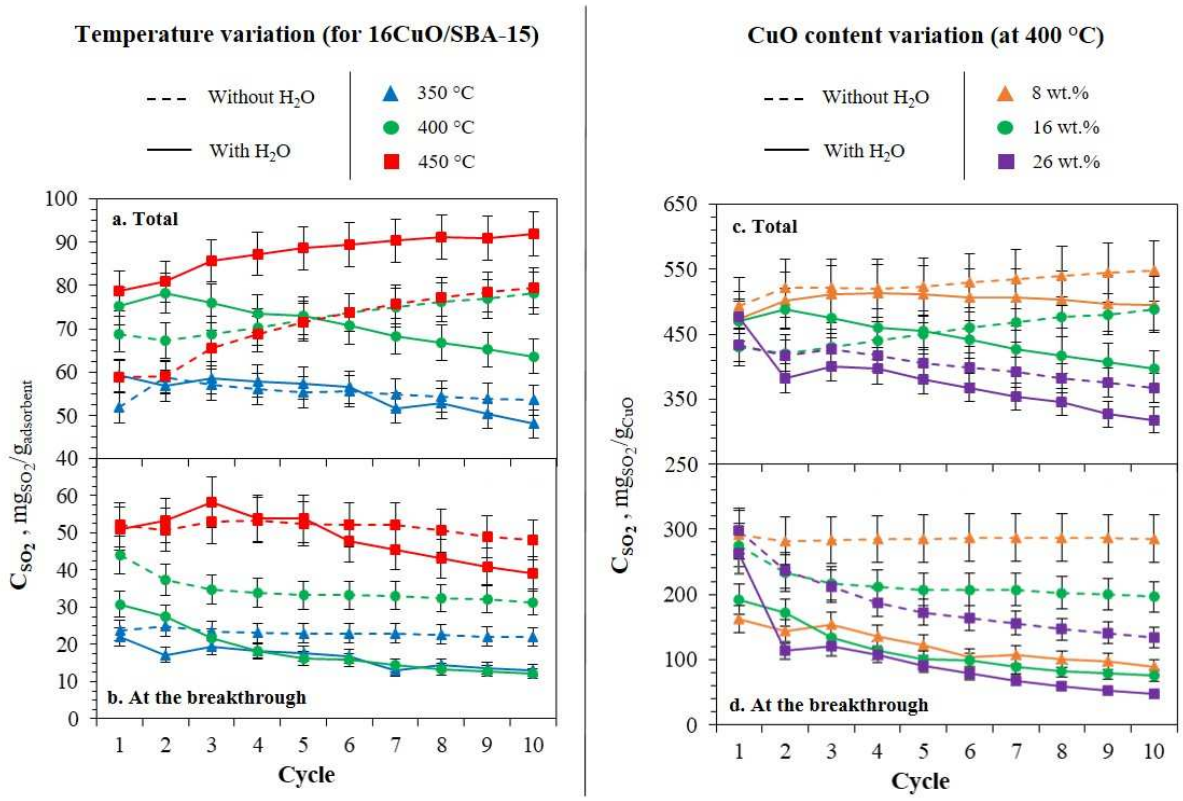

FIGURE 4

Evolution of the SO_2 adsorption capacities at the breakthrough and the total SO_2 adsorption capacities of the CuO/SBA-15 adsorbents, submitted to ten SO_2 adsorption/regeneration cycles with and without H_2O during the adsorption step. Left: 16CuO/SBA-15 adsorbent at 350 °C, 400 °C and 450 °C, right: 8, 16 and 26CuO/SBA-15 adsorbents at 400 °C.

During SO_2 adsorption steps without H_2O (**Figure 3a**), all the obtained SO_2 breakthrough curves are relatively similar (excepted for cycle 1). These curves indicate that after around 2 000 s, SO_2 begins to be detected in the output gas stream and its concentration increases and reaches a plateau at 185 ppm, while 250 ppm is still injected. As previously explained [10–13,20], this difference between the injected and the emitted values of SO_2 indicates that the copper based active phase is still able to oxidize SO_2 to SO_3 (this latter not being detected by the analyzer) at the end of the adsorption step, despite its progressive saturation due to the formation of copper sulphates. Excepted for cycle 1 where the SO_2 breakthrough occurs at about 3 000 s, the DeSOx performance of the adsorbent is relatively similar along cycles, in terms of SO_2 breakthrough curve profile (**Figure 3a**) and SO_2 adsorption capacity of the adsorbent at the breakthrough $C_{SO_2}^{breakthrough}$ (**Figure 4b**), as already observed in these operating conditions [11–13]. During the first cycle, it is assumed that the copper active phase is chemically

modified and stabilized during the following cycles [31]. Nevertheless, it can be observed a slightly decrease of the $C_{SO_2}^{breakthrough}$ (**Figure 4b**) from 37 to 33 $mg_{SO_2}/g_{adsorbent}$ from cycle 2 to cycle 6 and then a stabilization of the SO_2 adsorption capacity until cycle 10. This could be due to a partial agglomeration of copper active species after several cycles into larger particles (as it will be discussed in next section). Indeed, Centi *et al*. have mentioned that sulphation of CuO particle cores, is negatively affected by the fast formation of superficial copper sulphates, characterized by a cell volume higher than the one of CuO, which slow down the formation of further subsurface sulphate species [32].

On the other hand, in the presence of H_2O, the SO_2 breakthrough curves at 400°C show earlier SO_2 emissions along all cycles **(Figure 3b)**, and therefore, the $C_{SO_2}^{breakthrough}$ are lower than the ones observed without H_2O (12 $mg_{SO_2}/g_{adsorbent}$vs 31 $mg_{SO_2}/g_{adsorbent}$ for the tenth cycle) **(Figure 4b)**. Compared to the result without H_2O, a loss of 61 % of performance in SO_2 trapping at the breakthrough is observed at the tenth cycle. The evolution of the shape of the SO_2 breakthrough curves is also different in the presence of H_2O. Indeed, the slope of these curves becomes steeper along cycles. All these observations traduce the negative impact of the presence of H_2O in respect to the reaction of oxidation of SO_2 in SO_3, reaction catalyzed by the copper active phase. One possible explanation is that H_2O molecules could interact with copper active sites by forming hydroxyl copper species less or not reactive for the oxidation of SO_2 in SO_3, as assumed by Liu *et al*. [23] for the irreversible deactivation in $DeNO_x$ of Cu-Mn/SAPO-34 catalyst. Thus, a competitive adsorption on the copper active sites between H_2O and SO_2 molecules and therefore, the decrease of the number of copper active sites able to oxidize SO_2 in SO_3, may explain the observed deactivation of the CuO/SBA-15 adsorbent. Other possible causes for this decrease of performance, are the incomplete regeneration of the adsorbent along regeneration step or a more pronounced agglomeration of the copper active phase in presence of water vapor, as it will be discussed afterwards.

The SO_2 regeneration curves of the adsorbent after adsorption steps without H_2O in the gas stream exhibit two stages: a first very short one, with SO_2 emissions up to 2 700 ppm at around 40 s and a second one where SO_2 emissions are slow down and generate a plateau at around 1 800 ppm, which

duration increases over cycles (**Figure 3c**). This behavior can be explained by the fast decomposition of the most accessible copper sulphates that are located on the surface of the copper active phase and the decomposition of the copper sulphates present in the core of the copper active phase slowed down by diffusional limitations, respectively [11]. A slight increase of $C_{SO_2}^{total}$ along cycles, from 69 to 78 $mg_{SO_2}/g_{adsorbent}$ **(Figure 4a)** is observed, probably due to an increase of the Cu^+ species in the copper active phase, which seem to be the most copper active sites in SO_x trapping [10,11,33]. Indeed, the XRD analysis after 10 cycles showed the presence of the Cu_2O phase (*vide infra,* **Figure 7b).** The addition of H_2O in the flue gas changes drastically the profile of the desorption curves (**Figure 3d**). The intensity of the first sharp peak decreases and the SO_2 emissions are delayed, along the regeneration cycles. This trend could be explained by the formation of copper hydroxide species [23,24] on the surface sites of the copper active phase inhibiting their sulphation. It could be also due to the formation of surface hydrated copper sulphates such as the basic copper sulphate monohydrate ($CuO.CuSO_4.2Cu(OH)_2.H_2O$) for which the anhydrous part is stable up to 400 °C [34] or copper oxysulphates, that are difficult to regenerate under experimental conditions (400 °C, 0.5 vol.% H_2) [35]. Thus a decrease of $C_{SO_2}^{total}$ up to 19 % at the tenth cycle compared to the one obtained without water, is observed (**Figure 4a**). However, it appears that $C_{SO_2}^{total}$ is higher than the ones obtained without H_2O for the four first cycles, with an average gain of 12 %. Indeed, the presence of water could also lead to the formation of sulphite/sulphate species (SO_3^{2-}/SO_4^{2-}) at the easily accessible surface of the copper particles, which results in an increase of the sulphation reaction rate as shown by Osaka *et al* [26]. Nevertheless, this promoter effect seems to be inhibited along the cycles, perhaps by the decrease of the surface copper active sites, which are difficult to regenerate under experimental conditions as shown by the decrease in intensity and the disappearance of the first peak of the regeneration curves (**Figure 3d**).

3.1.2. Impact of the temperature on the SOx trapping performance of the 16CuO/SBA-15 adsorbent under wet conditions

In order to evaluate the influence of the temperature on the SOx trapping performance of the 16CuO/SBA-15 adsorbent under wet conditions, cyclic $DeSO_x$ tests were also realized with and without H_2O, at 350 °C (**Figures SI-1a, b, c and d**) and 450 °C (**Figures SI-1e, f, g and h).**

In comparison to the SO_2 adsorption tests at 400 °C (**Figure 3b**), the SO_2 breakthrough at 350 °C under wet conditions (5 vol. % of H_2O) (**Figure S2-1b**) appears earlier. This result traduces a decrease of the SO_2 breakthrough adsorption capacity $C_{SO_2}^{breakthrough}$ of 47 % at the tenth cycle compared to the one obtained without H_2O (**Figure 4b**). At 450 °C, the decrease of the $C_{SO_2}^{breakthrough}$ is lower (19 % at the tenth cycle) (**Figure 4b**). It is noteworthy that the overall shape of the SO_2 breakthrough curves is roughly similar whatever the humidity rate (0 or 5 vol.%) in the flue gas for 350 °C and 400 °C (**Figures SI-1a and b, Figures 3a and b**), whereas it changes at 450°C (**Figures SI-1e and f**). This shape evolution of the breakthrough curves at 450°C might be explained by more important chemical modifications of the copper active phase along cycles with the increase of the temperature, as shown from the TEM characterizations presented below. At the end of the adsorption phase, without H_2O, SO_2 emission reaches 220 ppm at 350 °C (**Figure S2-1a**), 185 ppm at 400°C (**Figure 3a**) and less than 80 ppm at 450 °C (**Figure S2-1e**). As expected, the increase of the temperature leads to a higher SO_2 oxidation reaction rate, which implies ~~a~~ higher SO_3 emissions. Under wet conditions (5 vol. % H_2O), at 350 °C (**Figure S2-1b**) and 400 °C (**Figure 3b**), the SO_2 emissions at the end of the adsorption steps remain equivalent to those measured without H_2O, whereas at 450 °C (**Figure S2-1f**), they increase strongly up to 160 ppm (i.e, an increase of 100 % compared to SO_2 emissions without H_2O). This behavior probably indicates that at 450 °C with water vapor in the gas stream, the SO_2 oxidation reaction rate decreases with a low impact on the sulphation reaction rate, as shown by the $C_{SO_2}^{breakthrough}$ evolution along the cycles compared to the dry conditions (**Figure 4b**).

Under dry conditions, the shape of the desorption curves at 350 °C (**Figure S2-1c**) are similar to the ones obtained at 400 °C (**Figure 3c**) with two clearly visible stages. However, SO_2 emissions at 350°C are delayed along regeneration cycles suggesting that the surface copper active sites are difficult to be regenerated at this temperature. At 450 °C (**Figure S2-1g**), the desorption curves are different that the

ones obtained at 350 and 400°C, without the first sharp peak of SO_2 emissions. It seems that the sulphate copper decomposition occurs with more or less similar kinetics for both the surface and the core copper active sites. In the presence of H_2O, the two distinct components are still observed at 350 °C (**Figure S2-1d**) and 400 °C (**Figure 3d**) but the intensity of the first one decreases along the cycles for both temperatures. Indeed, as already discussed, the presence of H_2O has probably generated sulphur based copper species, which are mainly located on the surface of the copper active phase and do not totally decompose over cycles in these thermal conditions. Moreover, the delay of SO_2 emissions is more pronounced after adsorption steps with H_2O at 350 than 400°C and increases along cycles. Consequently, the activity of the sorbent material is decreasing along cycles (**Figure 4a**). The increase of the temperature up to 450 °C with or without water vapor, allows to increase the total SO_2 adsorption capacity of the 16CuO/SBA-15 adsorbent (**Figure 4a**). The decomposition of the sulphur based copper species formed is more effective at this higher temperature, for both the surface and the core copper active sites, and the SO_2 emissions regularly and slowly increase over cycles without delay with and without H_2O. However, in the presence of water vapor, an average gain of SO_2 adsorption capacity of 24 % at the tenth cycle is observed (**Figure 4a**). This behavior might be due to a better sulphation reaction by the presence of sulphite/sulphate species as suggested by Osaka *et al* [26], which can be decomposed under reductive atmosphere at this higher temperature.

3.1.3. Impact of the CuO loading on the SO_x trapping performance of the CuO/SBA-15 adsorbent under wet conditions

The second parameter studied to assess the performance of the CuO/SBA-15 SO_2 adsorbent under wet conditions was the CuO active phase loading. Thus, CuO/SBA-15 materials with lower (8 wt.%) and higher (26 wt.%) CuO content were synthetized and tested at 400 °C (8CuO/SBA-15: **Figures SI-1i, j, k and l and** 26CuO/SBA-15: **Figures SI-1m, n, o and p**), over 10 adsorption/regeneration cycles, with or without H_2O.

As expected**,** without H_2O during the adsorption step, the SO_2 breakthrough becomes longer with the increase of the CuO active phase content on the support, due to the increase of the amount of adsorption sites (**Figures SI-I and m, Figure 3a)**. However, the $C_{SO_2}^{breakthrough}$ (expressed in mg of adsorbed SO_2 per gram of CuO active phase) (**Figure 4d**) decreases with the increase of the CuO content and along cycles, especially for the 26CuO/SBA-15 adsorbent. This behavior could be related to the dispersion state of the CuO active phase which is probably better at low Cu loading and consequently favors the interaction of the copper species with the SBA-15 support to form more stable (Cu-O-Si) species [33,36,37]. Indeed, the $C_{SO_2}^{breakthrough}$ evolution of the 8CuO/SBA-15 adsorbent (**Figure 4d**) stay stable over cycles (290 mg_{SO_2}/g_{CuO}). Unsurprisingly, with H_2O, the SO_2 breakthrough appears earlier whatever the CuO content in the adsorbent. Nevertheless, the 8CuO/SBA-15 adsorbent presents the higher loss of $C_{SO_2}^{breakthrough}$ (expressed here in mg_{SO_2}/g_{CuO}) of around 71 % (63 % and 61 % for 16CuO/SBA-15 and 26CuO/SBA-15, respectively) in the presence of water vapor at the tenth cycle (**Figure 4d**). This might be explained by its better CuO phase dispersion on the SBA-15 support that is more affected in terms of reactivity with H_2O.

An increase of the regeneration time (i.e. 1800 s) was applied to insure the complete decomposition of the sulphur based copper species for the higher CuO content (26 wt.%) adsorbent. Under dry conditions, the shape of the desorption curves of the 8CuO/SBA-15 shows a higher contribution of the first component attributed to the decomposition of surface sulphated copper active sites. This is in good agreement with a better dispersion of the CuO active phase on the SBA-15 support. When the CuO content increases, the contribution of the first component is reduced with besides an increase of the contribution of the second component related to the core sulphated copper species. In the presence of water molecules, as already discussed for the 16CuO/SBA-15, the contribution of the first component decreases drastically whatever the CuO content, the impact of H_2O on the total SO_2 adsorption capacity is similar: a slight decrease of the performance is observed along the adsorption/regeneration cycles. It is noteworthy that the total SO_2 adsorption capacity after the tenth cycle with or without H_2O, is higher for the lowest CuO content adsorbent (547 and 495 mg_{SO_2}/g_{CuO} without and with H_2O, respectively)

while it is lower for the highest CuO content adsorbent (367 and 318 mg_{SO_2}/g_{CuO}without and with H_2O, respectively) (**Figure 4c**). Some diffusional limitations of reacting gas into the particles of copper species probably slow down the reaction rates of sulphation and regeneration of the copper active sites. Such limitations seem to become predominant with the increase of the CuO loading and are strenghtened in the presence of water. This hypothesis will be validated by TEM analyses in next paragraph.

3.2. Structural and textural properties of the fresh and spent adsorbents

The adsorbents after the SO_2 adsorption/regeneration cycles (spent adsorbents) have been characterized by TEM, XRD and N_2 physisorption manometry and the data have been compared to those of the adsorbents before DeSOx experiments (fresh adsorbents). The TEM images **(Figures 5 and 6)** of the fresh CuO/SBA-15 adsorbents, whatever the CuO content, show only the ordered mesostructure characteristic of SBA-15 silica materials with parallel fringes corresponding to the cylindrical mesopores packed in 2D-hexagonal arrangement. The presence of CuO is not highlighted by this technique probably due to a good dispersion of the initial active species on the SBA-15 support as shown on EDX mappings of copper. As mentioned in previous study [10], the deposited copper active phase is probably under the form Cu^{2+}-O-Si, species in strong interaction with the support. After ten SO_2 adsorption/regeneration cycles at 400 °C with and without H_2O, the presence of nanoparticles is clearly observed on the 16CuO/SBA-15 adsorbent (**Figure 5**). These nanoparticles seem mainly regularly dispersed in the mesopores of the SBA-15 support when SO_2 adsorption/regeneration cycles were performed without H_2O. They are probably formed as a result of the migration of the copper active species into the mesoporosity upon $DeSO_x$ tests that interact to assemble each other. In the presence of H_2O, the nanoparticles appear slightly larger but are still regularly dispersed within the cylindrical mesopores or on the surface of the SBA-15 support. The presence of particles on the support surface might be the result of a further migration of copper active species towards the pore entrances. When the adsorption/regeneration step is performed at 350 °C, similar observations can be done. However at 450 °C, the migration of the copper active species is favored and becomes dominant in the presence of H_2O that probably promotes, by forming silanol groups (Si-OH) on the SiO_2 support, the mobility of the

copper active phase and the coalescence of the copper species to generate mainly large particles of size around 50 nm on the SBA-15 support surface as already observed in the Pd/SiO_2 system by Lamber *et al.* [38]. At low CuO concentration, no particle is observed for the 8CuO/SBA-15 material after SO_2 adsorption/regeneration cycles at 400 °C under dry conditions (**Figure 6**). This highlight the good dispersion of the CuO species on the adsorbent as assumed to explain the high proportion of surface active sites (see regeneration curves in **Figure S2-1k**). In the presence of water vapor, small copper species particles homogeneously dispersed along mesopores are observed because of the favored migration of the copper species in these conditions. Besides these small particles, some larger ones, outside the mesopores, can also be observed. After $DeSO_x$ tests at 400 °C without H_2O, when the CuO loading is increased up to 26 wt% (**Figure 6**) large copper species particles of about 50-70 nm on the SBA-15 support surface are mainly observed in coexistence with few particles whose size fit with mesopore size (around 6 nm). When H_2O is added to the flue gas, the 26CuO/SBA-15 adsorbent after ten SO_2 adsorption/regeneration cycles presents few very big spherical particles with average size varying from 50 to 150 nm. Few small particles located on the surface or within the mesopores are also observed.

The TEM analyses show that SO_2 adsorption/desorption tests induce copper species migration that interact to form larger particles in the cylindrical mesopores and/or on the surface of the SBA-15 support. The presence of H_2O favors the copper species migration and thus the particle growth**.**

The growth of copper species particles observed with both the temperature and the CuO loading increase, as well as the presence of H_2O, implies a decrease of the surface/volume ratio of these particles. Thus, the ratio of accessible surface copper species to less accessible core copper species could explain the evolution of the shape of the adsorption and desorption curves.

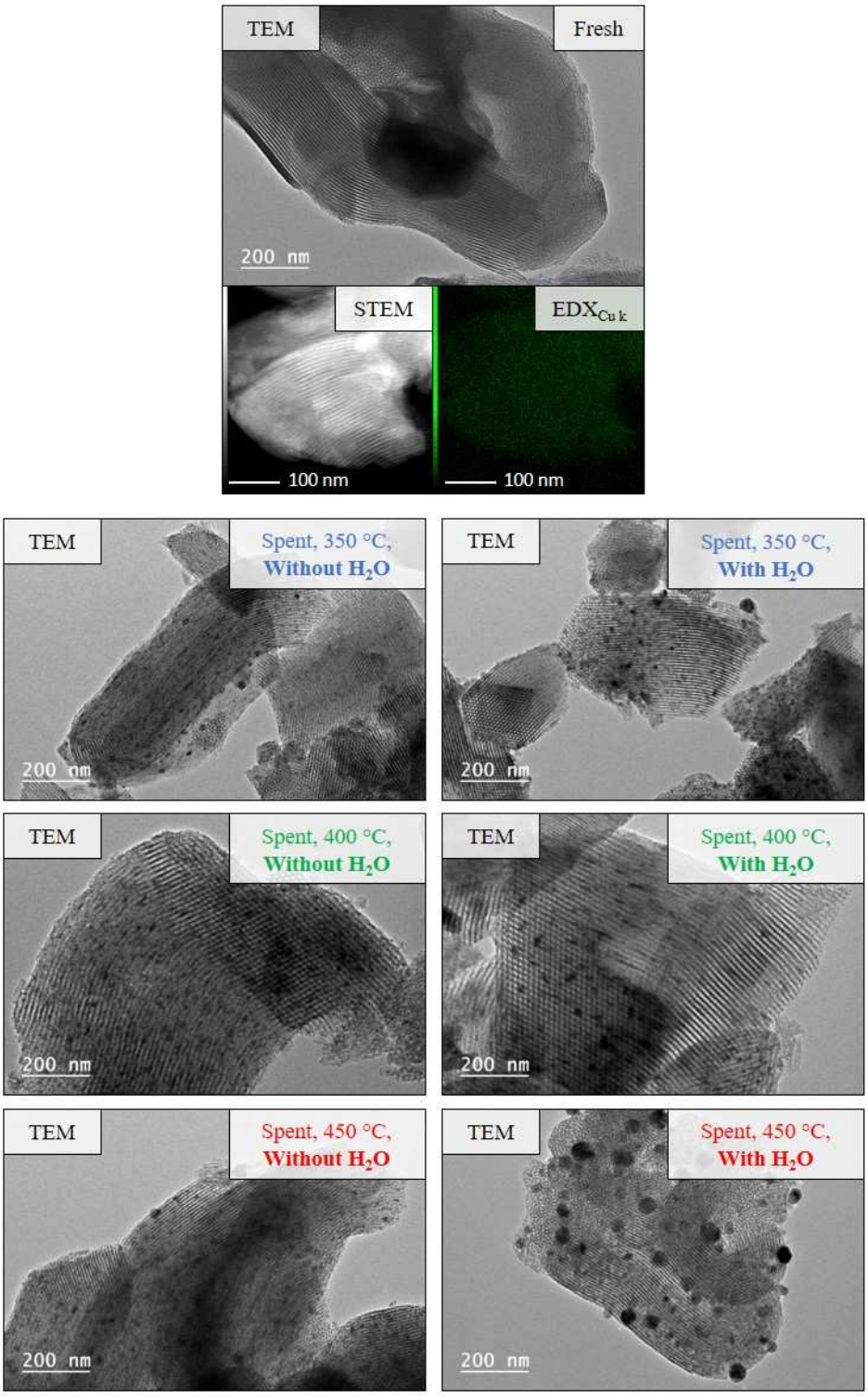

FIGURE 5

TEM micrographs, STEM micrographs and EDX mappings (Cu) of the fresh and spent 16CuO/SBA-15 adsorbents, submitted to ten adsorption/regeneration cycles, at 350 °C, 400 °C and 450 °C, with or without H_2O during the adsorption step.

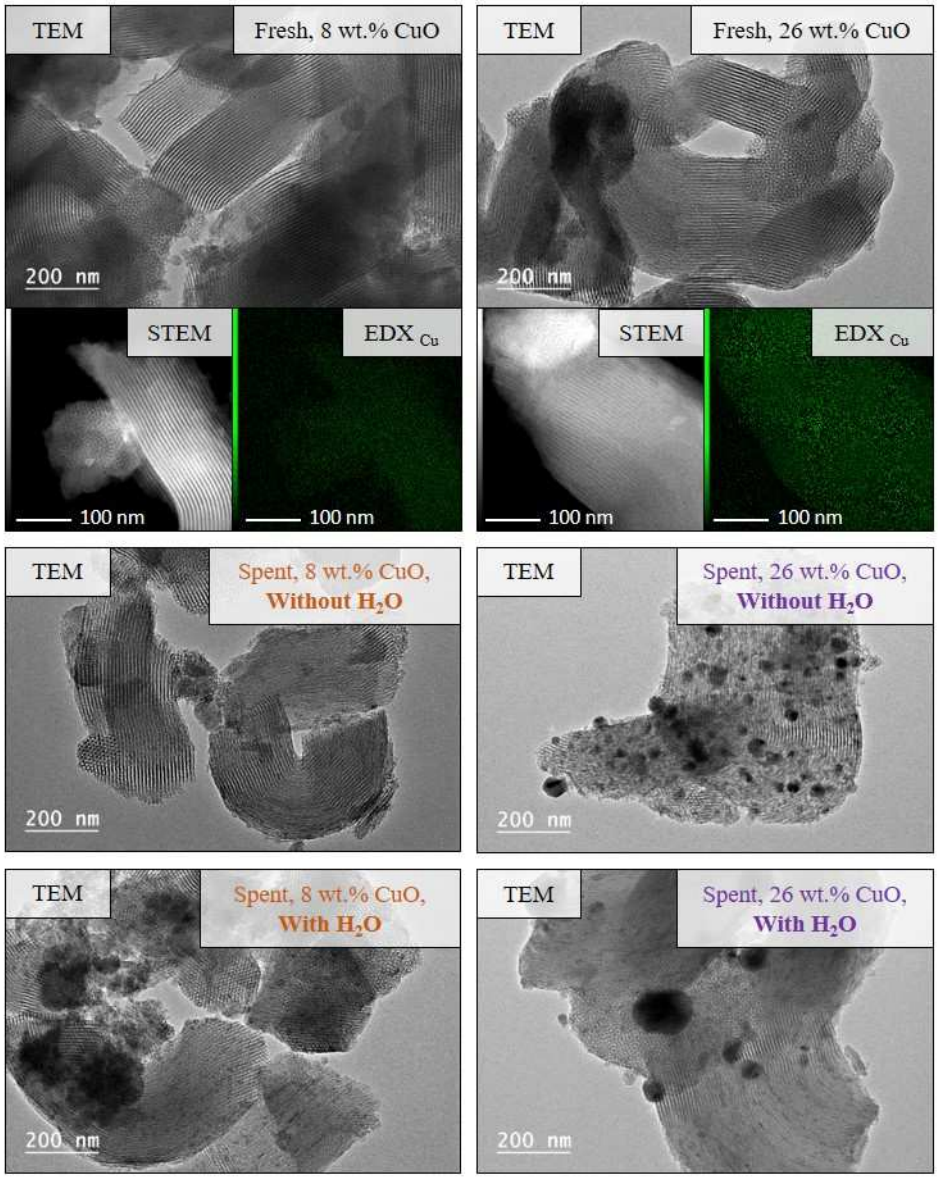

FIGURE 6

TEM micrographs, STEM micrographs and EDX mappings (Cu) of the fresh and spent 8CuO/SBA-15 and 26CuO/SBA-15 adsorbents, submitted to ten adsorption/regeneration cycles, at 400 °C, with or without H_2O during the adsorption step.

The three diffraction peaks observable on the low-angle XRD patterns of the fresh CuO/SBA-15 adsorbents (**Figures 7a and c**) at around 1°, 1.6° and 1.8°, can be indexed in the (100), (110) and (200) reflection planes that are characteristics of a 2D-hexagonal structure as expected for the SBA-15 support. After cyclic SO_2 adsorption/regeneration tests, with and without H_2O and whatever the temperature and the CuO loading, the mesostructure is preserved but with a slight reduction of the hexagonal lattice parameter (values reported in **Table 1**). This is assigned to a shrinkage of the silica network due to the

dehydroxylation reactions upon cyclic $DeSO_x$ test conditions [37,39,40]. Except for the 16CuO/SBA-15 and 8CuO/SBA-15 adsorbents, after $DeSO_x$ tests at 350 °C and 400 °C, respectively, the wide-angle XRD patterns (**Figures 7b and d**) of the spent CuO/SBA-15 adsorbents display peaks that are attributed to the Cu^0 and Cu_2O crystalline structures. The XRD peaks are thinner and more intense when the temperature of the cyclic SO_2 adsorption/regeneration tests increases and also with the increase of the CuO active phase content of the adsorbent, indicating the presence of larger particles as observed by TEM and higher degree of crystallization. It is noteworthy that no clear effect of the presence of water on the copper active species can be detected on the XRD patterns. For the 16CuO/SBA615 after $DeSO_x$ test at 350 °C and for the 8CuO/SBA-15 adsorbent tested at 400 °C it is assumed that the crystallization rate is too low and/or the crystalline domains are too small to be detected by the XRD technique.

The nitrogen adsorption/desorption isotherms of the fresh and the spent CuO/SBA-15 adsorbents, with and without H_2O**,** and their textural characteristics are reported in **Figure 8** and **Table 1**, respectively.

All N_2 physisorption isotherms of the SBA-15 support, of the fresh and spent adsorbents display a combination of type I(b) and IV(a) isotherms as expected for an ordered mesoporous silica material such as SBA-15 whose regular cylindrical mesopores are interconnected by micropores [41]. However, all fresh adsorbents exhibit a hysteresis loop with an elongation of the desorption branch towards low relative pressures, excepted for the SBA-15 support. The hysteresis loop is type H1, which is characteristic of cylindrical mesopores according to the IUPAC classification, while the elongation of the desorption branch is probably due to the presence of CuO active phase into the porosity. For the spent adsorbents, except the ones at 450 °C, in dry and wet conditions and after the ten SO_2 adsorption-regeneration cycles, the hystereses are type H5 since they present a sharp step-down of the desorption branch at a relative pressure p/p_0 of 0.45, more or less important depending on the applied temperature or the CuO loading. This hysteresis shape indicates a partial pore blocking that appears to be more important than the one observed on the fresh adsorbents. This phenomenon can be explained by the $DeSO_x$ test conditions, which lead to the migration and subsequent particle growth of copper species within the adsorbents as observed on wide angle XRD patterns (**Figure 7b**) and TEM images (**Figures**

5 and 6). Surprisingly, at 450 °C, no change in the profile of N_2 physisorption isotherms occurs before and after the SO_2 adsorption regeneration cycle. This might be explained by the formation of the large Cu-based particles on the surface of the adsorbent, which may release space in the mesoporosity of the 16CuO/SBA-15 adsorbent as shown on TEM images (**Figure 5**). The same trends on the physisorption isotherms are observed when the CuO loading increased from 8 wt.% to 26 wt.% (**Figure 8**). The evolution of the shape of the hysteresis loop as previously described, can be related to the copper particles size (**Figures 5, 6 and 8**). In all cases, whatever the SO_2 adsorption-regeneration temperature and the copper content on the CuO/SBA-15 adsorbent, a decrease in specific surface areas, microporous mesoporous volumes is observed after the SO_2 cycling experiments in dry and wet conditions compared to the fresh adsorbents. The same trend is observed between the SBA-15 pseudo-impregnated, calcined at 500 °C and shaped and of the fresh CuO/SBA-15 adsorbents but in this case, the decrease of the textural properties is due to the densification of the material. A decrease of the average pore diameters is also noticed (**Table 1**). Indeed, whatever the temperature used during the adsorption regeneration cycles and whatever the CuO loading, the two pore size distributions obtained for the fresh and spent adsorbents (**Figure SI-3**) present a decrease of the pore size more or less significant. For the experiments performed at 350 and 400°C a similar decrease in pore size is observed for the spent adsorbents after SO2 adsorption with and without water. This decrease can be linked to a partial pore blocking due to the agglomeration of copper species in the mesoporosity (**Figure 5**). At 450°C, the agglomeration of the copper species is enhanced, which leads to the formation of larger CuO particles which move outside the porosity (**Figure 5**), this phenomenon may explain the slight change in the pore size observed on the spent materials compared to one of the fresh one. Concerning the impact of the CuO loading on the pore size distribution after the adsorption-regeneration experiments with and without water, this one is low for the 8CuO/SBA-15 adsorbent compared to 16CuO/SBA-15 and 26CuO/SBA-15 adsorbents. This trend may be due to the low content of the copper species in the fresh adsorbent, which after SO_2 adsorption-regeneration cycles leads to the formation of very small particles of CuO (**Figure 6**). Therefore, a temperature of 450 °C and a CuO loading of 26 wt.% impact drastically the textural properties of the CuO/SBA-15 adsorbents after the successive SO_2 adsorption regeneration cycles. It is noteworthy that the presence of water does not seem to induce important change on the textural

properties of the spent adsorbents while the TEM analysis clearly shows that the presence of water in the flue gas leads to the formation of larger copper species particles located within mesopores but mainly on the surface of the support.

4. Conclusion

The aim of this study was to evaluate the effect of water vapor on the SO_2 adsorption capacities at the breakthrough and the total SO_2 adsorption capacities of CuO/SBA-15 adsorbents. Globally, it was showed that the presence of H_2O in the flue gas generates a loss of activity in SO_2 trapping. The potential causes could be:

- the blocking of the Cu-based active sites by competitive physisorption of the H_2O and SO_2 molecules
- the formation of copper based sulphate species difficult to decompose and the agglomeration of the active phase along cycles.

However, a significant promoting effect of the presence of water vapor on the performance in SO_2 trapping is observed by increasing the temperature of the $DeSO_x$ process to 450 °C. At this temperature, it seems that the presence of H_2O influences the adsorption kinetics of SO_2 on the CuO active phase by enhancement of the SO_2 oxidation or by a possible formation of sulphite type intermediates, which react more easily with the copper active sites. Moreover, the increase in temperature could permit a better decomposition of the copper based sulphate species and thus the regeneration of the adsorbent.

This study also reveals that the adsorbent with a low copper content (8 wt. % of CuO), is more stable in terms of copper active phase dispersion, along cycling experiments, even in the presence of water vapor. This result demonstrates an interesting regeneration potential of this material for a possible future application at industrial level.

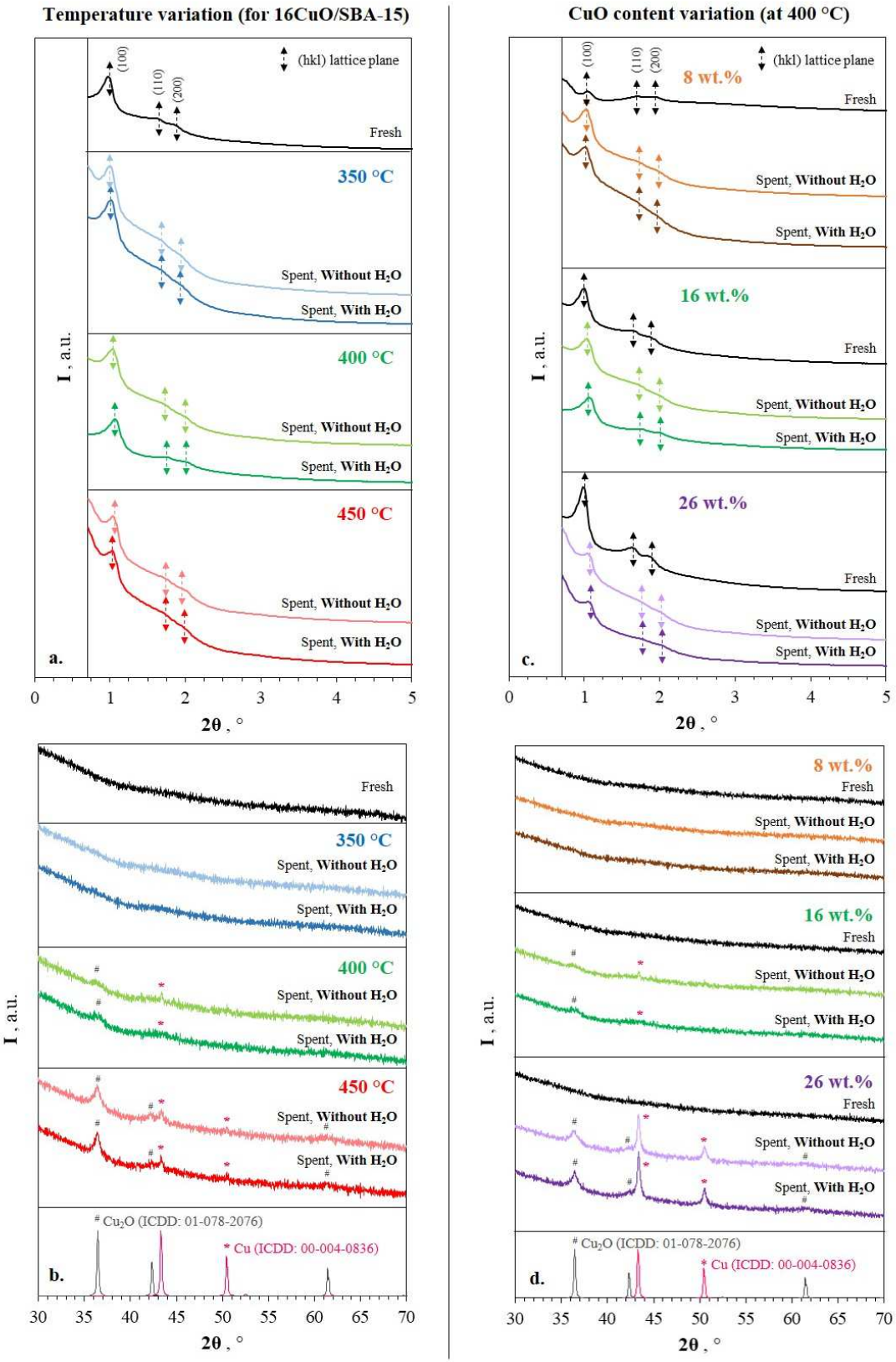

FIGURE 7

XRD patterns at low (a, c) and wide (b, d) 2θ angles ($Cu_{K\alpha}$ radiation) of the fresh and spent CuO/SBA-15 adsorbents, submitted to ten SO_2 adsorption/regeneration cycles with and without H_2O during the adsorption

step. Left: 16CuO/SBA-15 adsorbent at 350 °C, 400 °C and 450 °C, right: 8, 16 and 26CuO/SBA-15 adsorbents at 400 °C (Cu and Cu_2O XRD patterns from the International Centre for Diffraction Data).

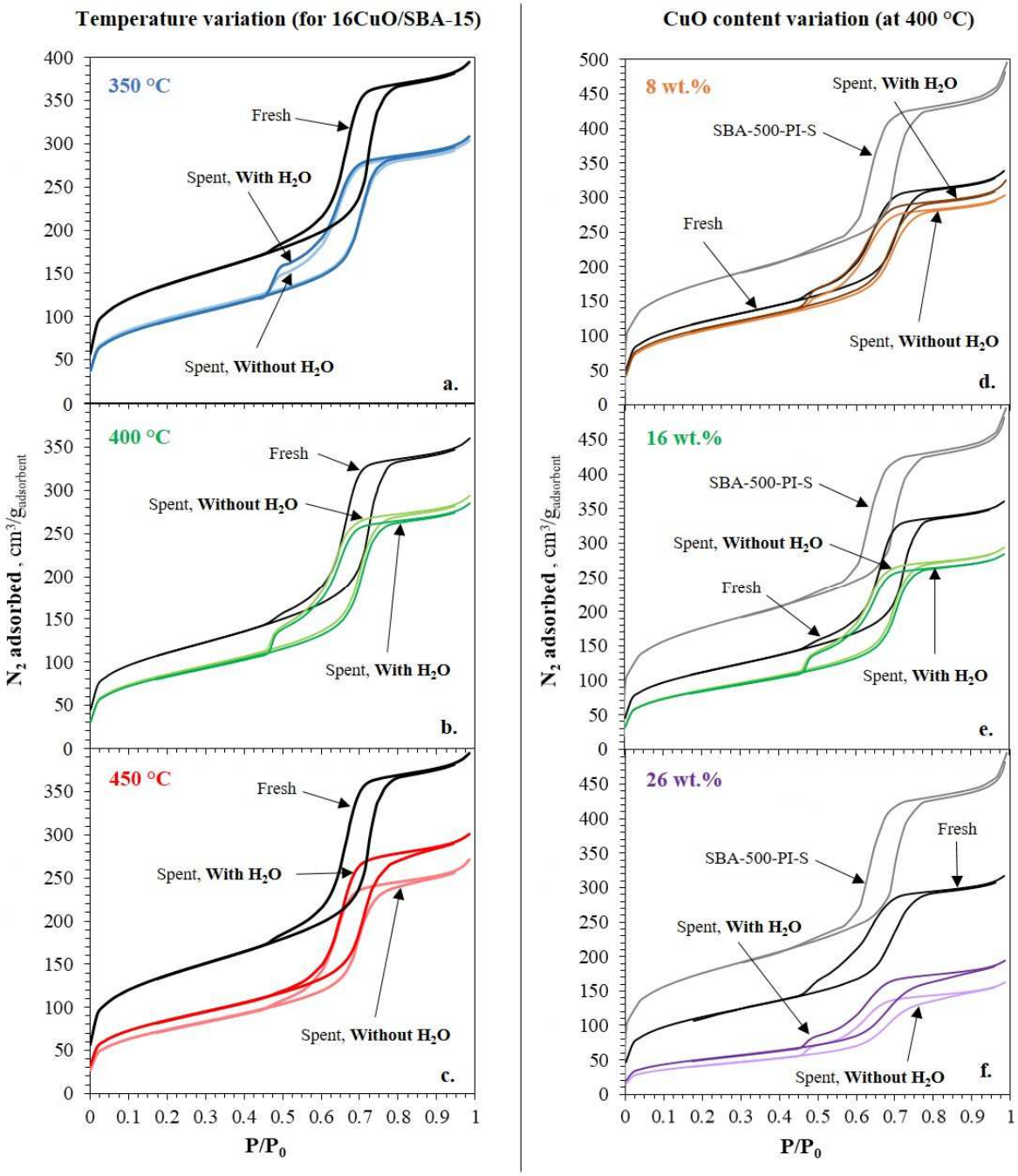

FIGURE 8

Nitrogen adsorption/desorption isotherms at -196 °C of the SBA-15 support pseudo-impregnated, calcined at 500 °C and shaped (SBA-500-PI-S) and of the fresh and spent CuO/SBA-15 adsorbents, submitted to ten SO_2 adsorption/regeneration cycles with and without H_2O during the adsorption step. Left: 16CuO/SBA-15 adsorbent at 350 °C, 400 °C and 450 °C, right: 8, 16 and 26CuO/SBA-15 adsorbents at 400 °C.

5. Acknowledgements

The authors want to gratefully acknowledge The French Environment and Energy Management Agency (ADEME), Zéphir Alsace S.A.S and the “Fondation pour l’ENSCMu” for their financial support. XRD analyses, nitrogen sorption measurements and TEM micrographs were performed on the technical platforms of IS2M.

6. References

[1] A. De Marco, C. Proietti, A. Anav, L. Ciancarella, I. D’Elia, S. Fares, M.F. Fornasier, L. Fusaro, M. Gualtieri, F. Manes, A. Marchetto, M. Mircea, E. Paoletti, A. Piersanti, M. Rogora, L. Salvati, E. Salvatori, A. Screpanti, G. Vialetto, M. Vitale, C. Leonardi, Environ. Int. 125 (2019) 320–333. https://doi.org/10.1016/j.envint.2019.01.064.

[2] J. Lelieveld, K. Klingmüller, A. Pozzer, U. Pöschl, M. Fnais, A. Daiber, T. Münzel, Eur. Heart J. 40 (2019) 1590–1596. https://doi.org/10.1093/eurheartj/ehz135.

[3] G.E. Likens, T.J. Butler, Acid Rain: Causes, Consequences, and Recovery in Terrestrial, Aquatic, and Human Systems, in: Encyclopedia of the Anthropocene, Elsevier, 2018: pp. 23–31. https://doi.org/10.1016/B978-0-12-809665-9.09977-8.

[4] A History Of Flue Gas Desulfurization Systems Since 1850: Research, Development and Demonstration, J. Air Pollut. Control Assoc. 27 (1977) 948–961. https://doi.org/10.1080/00022470.1977.10470518.

[5] T. Lecomte, J.F. Ferrería de la Fuente, F. Neuwahl, M. Canova, A. Pinasseau, I. Jankov, T. Brinkmann, S. Roudier, L. Delgado Sancho, Best Available Techniques (BAT) - Reference document for large combustion plants: industrial emissions directive 2010/75/EU - Integrated

pollution prevention and control, European Commission, 2017. http://eippcb.jrc.ec.europa.eu (accessed April 15, 2019).

[6] Commission économique pour l'Europe, Protocole de Göteborg de 1999 à la convention sur la pollution atmosphérique transfrontière à longue distance, relatif à la réduction de l'acidification, de l'eutrophisation et de l'ozone troposphérique, amended on 04 May 1992, 2013. https://www.unece.org (accessed March 31, 2019).

[7] Le Parlement Européen et le Conseil de l'Union Européenne, Directive (eu) 2016/2284 du parlement européen et du conseil du 14 décembre 2016, 2016. http://data.europa.eu (accessed March 22, 2019).

[8] Y. Mathieu, M. Soulard, J. Patarin, M. Molière, Fuel Process. Technol. 99 (2012) 35–42. https://doi.org/10.1016/j.fuproc.2012.02.005.

[9] Y. Mathieu, L. Tzanis, M. Soulard, J. Patarin, M. Vierling, M. Molière, Fuel Process. Technol. 114 (2013) 81–100. https://doi.org/10.1016/j.fuproc.2013.03.019.

[10] M. Berger, P. Fioux, S. Dorge, H. Nouali, D. Habermacher, E. Fiani, M. Vierling, J. Patarin, J.-F. Brilhac, Catal. Sci. Technol. 7 (2017) 4115–4128. https://doi.org/10.1039/C7CY01010A.

[11] M. Berger, H. Nouali, S. Dorge, D. Habermacher, E. Fiani, M. Vierling, M. Molière, C. Schönnenbeck, J.-F. Brilhac, J. Patarin, Chem. Eng. J. 347 (2018) 202–213. https://doi.org/10.1016/j.cej.2018.04.066.

[12] M. Berger, S. Dorge, H. Nouali, D. Habermacher, E. Fiani, M. Vierling, M. Molière, J.F. Brilhac, J. Patarin, Chem. Eng. J. 350 (2018) 729–738. https://doi.org/10.1016/j.cej.2018.05.170.

[13] M. Berger, S. Dorge, H. Nouali, D. Habermacher, E. Fiani, M. Vierling, M. Molière, J.F. Brilhac, J. Patarin, Chem. Eng. J. 384 (2020) 123318. https://doi.org/10.1016/j.cej.2019.123318.

[14] P. Shah, V. Ramaswamy, Micropor. Mesopor. Mat. 114 (2008) 270–280. https://doi.org/10.1016/j.micromeso.2008.01.013.

[15] X. Zhang, G. Zhuang, J. Chen, Y. Wang, X. Wang, Z. An, P. Zhang, J. Phys. Chem. B. 110 (2006) 12588–12596. https://doi.org/10.1021/jp0617773.

[16] D. Zhao, J. Feng, Q. Huo, N. Melosh, G.H. Fredrickson, B.F. Chmelka, G.D. Stucky, Science. 279 (1998) 548–552. https://doi.org/10.1126/science.279.5350.548.

[17] W.G. Davenport, M.J. King, B. Rogers, A. Weissenberger, Sulphuric Acid Manufacture, in: R.T. Jones, Johannesburg, 2006: p. 16. http://www.saimm.co.za/Conferences/Pyro2006/.

[18] W.G. Davenport, M.J. King, CHAPTER 2 - Production and Consumption, in: W.G. Davenport, M.J. King (Eds.), Sulfuric Acid Manufacture, Elsevier, Oxford, 2006: pp. 11–17. https://doi.org/10.1016/B978-008044428-4/50002-6.

[19] S.G. Nelson, Elemental sulfur production from SO_2-rich gases, in: B.K. Parekh, J.G. Groppo (Eds.), Coal Science and Technology, 1993: pp. 543–554. https://doi.org/10.1016/B978-0-444-81476-0.50047-8.

[20] M. Berger, A. Brillard, S. Dorge, D. Habermacher, H. Nouali, P. Kerdoncuff, M. Vierling, M. Molière, J. Patarin, J.-F. Brilhac, J. Hazard. Mater. 385 (2020) 121579. https://doi.org/10.1016/j.jhazmat.2019.121579.

[21] M. Iwamoto, N. Mizuno, H. Yahiro, Stud. Surf. Sci. Catal. 75 (1993) 1285–1298. https://doi.org/10.1016/S0167-2991(08)64451-1.

[22] W.S. Kijlstra, J.C.M.L. Daamen, J.M. Van de Graaf, B. Der Linden, E.K. Poels, A. Bliek, Appl. Catal. B. 7 (1996) 337–357. https://doi.org/10.1016/0926-3373(95)00052-6.

[23] G. Liu, W. Zhang, P. He, S. Guan, B. Yuan, R. Li, Y. Sun, D. Shen, Catalysts. 9 (2019) 289. https://doi.org/10.3390/catal9030289.

[24] R. Gholami, M. Alyani, K. Smith, Catalysts. 5 (2015) 561–594. https://doi.org/10.3390/catal5020561.

[25] Z. Wu, H. Zhu, Z. Qin, H. Wang, J. Ding, L. Huang, J. Wang, Fuel. 104 (2013) 41–45. https://doi.org/10.1016/j.fuel.2010.03.001.

[26] Y. Osaka, K. Iwai, T. Tsujiguchi, A. Kodama, H. Huang, Environ. Technol. (2019) 1–7. https://doi.org/10.1080/09593330.2019.1614095.

[27] C. Laguerie, D. Barreteau, Sadhana. 10 (1987) 49–67. https://doi.org/10.1007/BF02816197.

[28] S. Brunauer, P.H. Emmett, E. Teller, J. Am. Chem. Soc. 60 (1938) 309–319. https://doi.org/10.1021/ja01269a023.

[29] A. Galarneau, F. Villemot, J. Rodriguez, F. Fajula, B. Coasne, Langmuir. 30 (2014) 13266–13274. https://doi.org/10.1021/la5026679.

[30] E.P. Barrett, L.G. Joyner, P.P. Halenda, J. Am. Chem. Soc. 73 (1951) 373–380. https://doi.org/10.1021/ja01145a126.

[31] C.S. Shin, H. Niiyama, J. Japan Pet. Inst. 31 (1988) 147–153. https://doi.org/10.1627/jpi1958.31.147.

[32] G. Centi, N. Passarini, S. Perathoner, A. Riva, Ind. Eng. Chem. Res. 31 (1992) 1947–1955. https://doi.org/10.1021/ie00008a016.

[33] P. Gaudin, P. Fioux, S. Dorge, H. Nouali, M. Vierling, E. Fiani, M. Molière, J.-F. Brilhac, J. Patarin, Fuel Process. Technol. 153 (2016) 129–136. https://doi.org/10.1016/j.fuproc.2016.07.015.

[34] I. Uzunov, D. Klissurski, L. Teocharov, J. Therm. Anal. Calorim. 44 (1995) 685–696. https://doi.org/10.1007/BF02636286.

[35] G. Lachenal, J.R. Vignalou, Thermochimica Acta. 64 (1983) 207–227. https://doi.org/10.1016/0040-6031(83)80144-0.

[36] P. Gaudin, S. Dorge, H. Nouali, M. Vierling, E. Fiani, M. Molière, J.-F. Brilhac, J. Patarin, Appl. Catal. B. 181 (2016) 379–388. https://doi.org/10.1016/j.apcatb.2015.08.011.

[37] P. Gaudin, L. Michelin, L. Josien, H. Nouali, S. Dorge, J.-F. Brilhac, E. Fiani, M. Vierling, M. Molière, J. Patarin, Fuel Process. Technol. 148 (2016) 1–11. https://doi.org/10.1016/j.fuproc.2016.02.025.

[38] R. Lamber, N. Jaeger, G. Schulz-Ekloff, J. Catal. 123 (1990) 285–297. https://doi.org/10.1016/0021-9517(90)90128-7.

[39] T. Benamor, L. Michelin, B. Lebeau, C. Marichal, Micropor. Mesopor. Mat. 147 (2012) 334–342. https://doi.org/10.1016/j.micromeso.2011.07.004.

[40] F. Bérubé, S. Kaliaguine, Micropor. Mesopor. Mat. 115 (2008) 469–479. https://doi.org/10.1016/j.micromeso.2008.02.028.

[41] M. Thommes, K. Kaneko, A.V. Neimark, J.P. Olivier, F. Rodriguez-Reinoso, J. Rouquerol, K.S.W. Sing, Pure Appl. Chem. 87 (2015) 1051–1069. https://doi.org/10.1515/pac-2014-1117.

TABLE 2

Structural and textural properties of the SBA-15 support pretreated or not and of the fresh and spent CuO/SBA-15 adsorbents.

Sample	Specific surface area[a] ($m^2/g_{adsorbent}$)	Porous volumes ($cm^3/g_{adsorbent}$)			Average pores diameters[e] (nm)	Hexagonal lattice parameter[f] (nm)	Wall thickness[g] (nm)
		Total[b]	Micro.[c]	Meso.[d]			
Support							
SBA-300	750	0.80	0.19	0.61	6.0	-	-
SBA-500	660	0.71	0.16	0.55	5.6	-	-
SBA-500-S	630	0.67	0.16	0.51	5.6	-	-
SBA-500-PI	640	0.70	0.16	0.54	5.7	-	-
SBA-500-PI-S	630	0.68	0.16	0.52	5.7	-	-
Fresh adsorbents							
8CuO/SBA-15	430	0.49	0.14	0.35	4.0 / 5.9	10.2	4.3
16CuO/SBA-15	400	0.53	0.13	0.40	4.1 / 6.3	10.5	4.2
26CuO/SBA-15	400	0.51	0.13	0.38	4.0 / 6.2	10.6	4.4
Spent adsorbents							
8CuO/SBA-15, 400 °C							
0 vol.% H_2O	380	0.45	0.13	0.32	4.0 / 5.7	10.2	4.5
5 vol.% H_2O	390	0.46	0.13	0.33	4.0 / 5.7	10.1	4.4
16CuO/SBA-15							
350 °C							
0 vol.% H_2O	350	0.45	0.11	0.34	4.0 / 5.9	10.3	4.3
5 vol.% H_2O	340	0.45	0.11	0.34	4.0 / 6.0	10.4	4.5
400 °C							
0 vol.% H_2O	310	0.43	0.10	0.33	3.9 / 5.8	10.1	4.3
5 vol.% H_2O	300	0.42	0.10	0.32	3.9 / 6.0	9.8	3.8
450 °C							
0 vol.% H_2O	270	0.39	0.09	0.30	4.1 / 5.9	10.1	4.2
5 vol.% H_2O	310	0.44	0.10	0.34	4.1 / 6.1	10.0	3.9
26CuO/SBA-15, 400 °C							
0 vol.% H_2O	210	0.33	0.07	0.26	3.8 / 5.9	9.9	4.0
5 vol.% H_2O	190	0.30	0.06	0.24	3.8 / 5.8	9.8	4.0

[h] *Determined by the BET method [28]*
[i] *Total porous volume determined from the N_2 adsorbed volume at $p/p_0 = 0.90$*
[j] *Microporous volume determined from the N_2 adsorbed volume at $p/p_0 = 0.005$ [29]*
[k] *Mesoporous volume calculated from the difference between the total porous volume and the microporous volume*
[l] *Determined by the BJH method on the desorption branch [30]*
[m] *Determined from low 2θ angles XRD pattern*
[n] *Calculated from the difference between the hexagonal lattice parameter and the pore diameter*

Supplementary Information

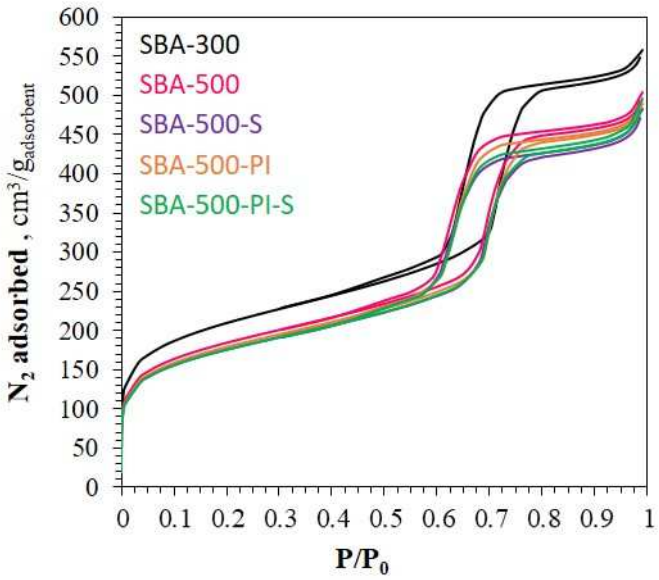

FIGURE SI-1

Nitrogen adsorption/desorption isotherms at -196 °C of the SBA-15 support calcined at 300 °C (SBA-300), at 500 °C (SBA-500), calcined at 500 °C and shaped (SBA-500-S), pseudo-impregnated and calcined at 500 °C (SBA-500-PI), pseudo-impregnated and calcined at 500 °C and shaped (SBA-500-PI-S).

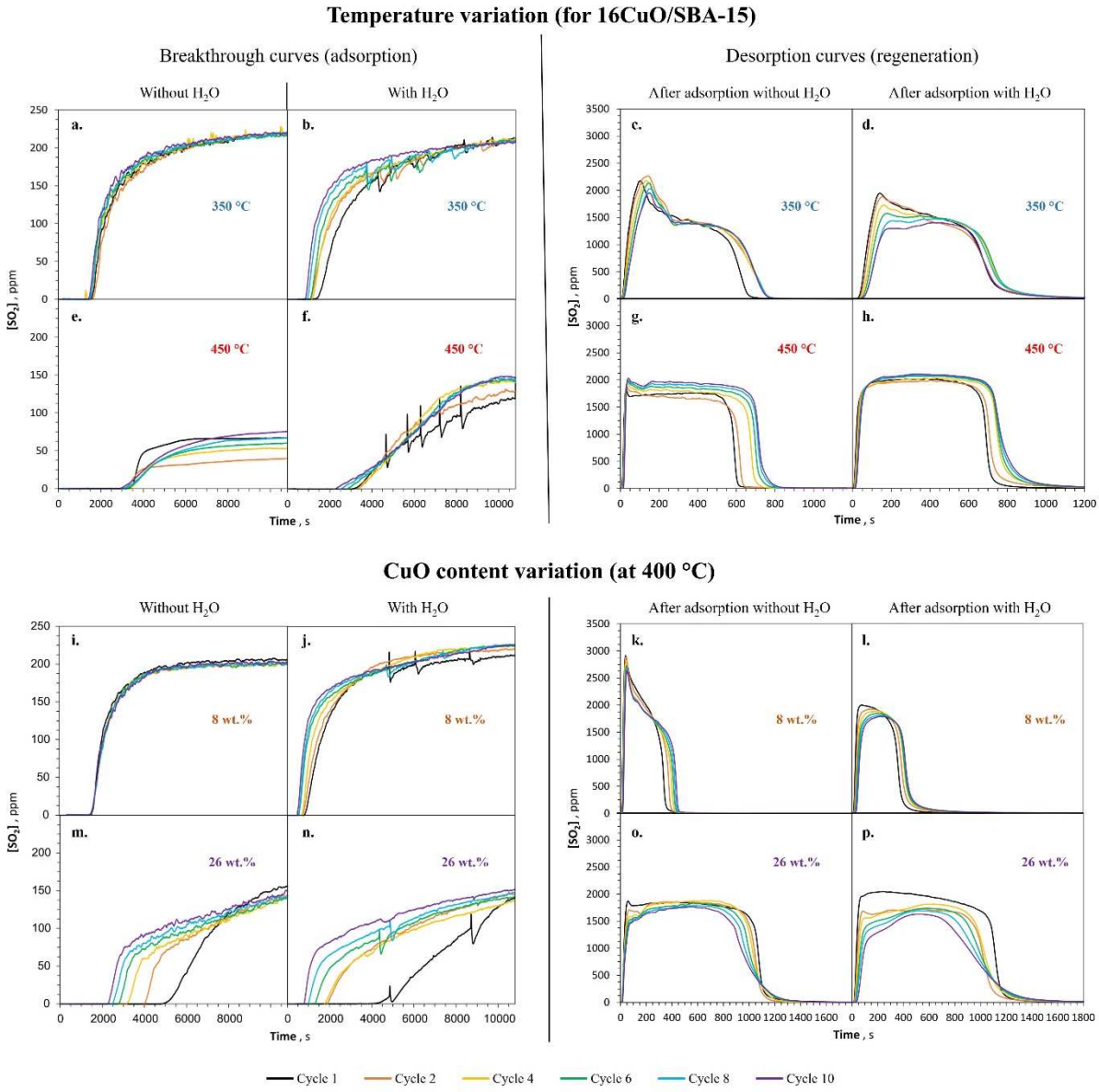

FIGURE SI-2

SO_2 breakthrough (left) and desorption (right) curves of the CuO/SBA-15 adsorbents, submitted to ten SO_2 adsorption/regeneration cycles with and without H_2O during the adsorption step. Top: 16CuO/SBA-15 adsorbent at 350 °C, 400 °C and 450 °C, bottom: 8 and 26CuO/SBA-15 adsorbents at 400 °C.

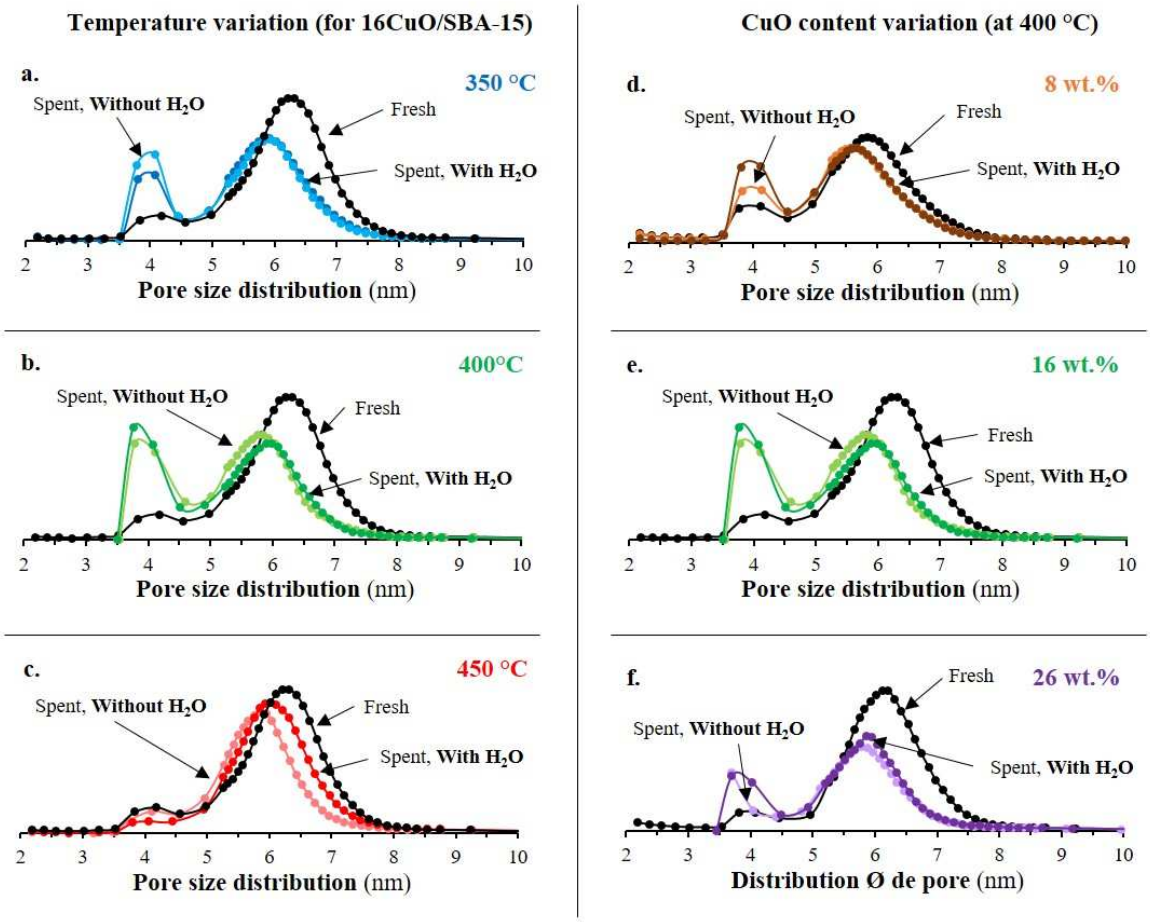

FIGURE SI-3

Pore size distributions of the fresh and spent CuO/SBA-15 adsorbents, submitted to ten SO_2 adsorption/regeneration cycles with and without H_2O during the adsorption step. Left: 16CuO/SBA-15 adsorbent at 350 °C, 400 °C and 450 °C, right: 8, 16 and 26CuO/SBA-15 adsorbents at 400 °C.